Inviscid Supersonic/Hypersonic Body Flowfield and Aerodynamics from Shock-Capturing Technique Calculations

D. S. Chaussee* and P. Kutler†
NASA Ames Research Center, Moffett Field, Calif.
and
T. Holtz‡
McDonnell Douglas Astronautics Co., Huntington Beach, Calif.

A shock-capturing, finite-difference computational procedure (SCT) has been used to predict the flowfields about various configurations for a wide range of initial conditions. The numerical results have been compared with wind tunnel data and show good agreement. Two different studies have been performed. In the first, details of the shock layer surrounding a space shuttle/orbiter configuration have been calculated. In the second, the aerodynamic forces and moments on a parametrically varied set of blunted biconic bodies of revolution have been evaluated for angles of attack up to 20° and Mach numbers from 5 to 20.

Nomenclature

BK = biconic break location along Z coordinate
C = constant used in meridional clustering
C_m = pitching moment coefficient, $M/q_\infty S_{\text{ref}} L_V$, about 0.65 L_V station
C_N = normal force coefficient, $N/q_\infty S_{\text{ref}}$
C_p = pressure coefficient, $(P-P_\infty)/q_\infty$
D = diameter
L = length of orbiter vehicle, ft
L_V = virtual length of aft cone, in.
L_α = length of biconic body, in.
M = Mach number
P = static pressure, lbf/ft^2
q = dynamic pressure, lbf/ft^2
r = cylindrical coordinate in radial direction
R = radius
Re = Reynolds number
S_{ref} = biconic body base area
Z,z = cylindrical coordinate in marching direction; for biconic body, axial coordinate measured from virtual apex of aft cone
Z_{CP} = axial center of pressure location on biconic body
α = angle of attack, deg
β = meridional clustering parameter
γ = ratio of specific heats
ζ = computational coordinate in marching direction
η = computational coordinate in meridional direction
θ_A = aft cone angle, deg
θ_F = fore cone angle, deg
ξ = transformed coordinate in radial direction
τ = computational coordinate in radial direction
ϕ = cylindrical coordinate in meridional direction
ω = radial clustering parameter

Subscripts

b = body
B = base
N = nose
ref = reference
s = shock
∞ = freestream conditions

Presented as Paper 75-837 at the AIAA 8th Fluid and Plasma Dynamics Conference, Hartford, Conn., June 16-18, 1975; received July 21, 1975; revision received Feb. 13, 1976. Work on biconic bodies was suported in part by Air Force Contract No. F04701-71-C-0048. R. A. Batchelder of McDonnell Douglas Astronautics Co. provided advice and assistance in the biconic computation study. The biconic wind tunnel tests were conducted under the direction of F. K. Hube and T. D. Buchanan of ARO, Inc. at the Arnold Engineering Development Center and K. F. Stetson at the Air Force Aerospace Research Labs.

Index categories: Supersonic and Hypersonic Flows; LV/M Aerodynamics.

*National Research Council Postdoctoral Fellow, Computational Fluid Dynamics Branch. Presently with Nielsen Engineering and Research, Inc., Mountain View, Calif. Member AIAA.

†Research Scientist, Computational Fluid Dynamics Branch. Associate Fellow AIAA.

‡Engineer/Scientist-Specialist. Presently with Aerotherm Div., Acurex Corp., Mountain View, Calif. Member AIAA.

Introduction

In the preliminary design of supersonic/hypersonic configurations, such as the space shuttle or other re-entry vehicles, a detailed description of the surrounding three-dimensional flowfield is important to the vehicle designer. Knowledge of the flowfield is necessary to predict the heat-transfer rates, aerodynamic loads, and boundary-layer effects. Intricate three-dimensional flowfields consisting of multiple shock waves, expansion waves, and contact surfaces, all interacting with each other, result when complex configurations travel through the earth's atmosphere at supersonic and hypersonic velocities. At present, there are a number of existing computer codes available for calculating such flowfields. In order to establish the credibility and increase the usefulness of a particular computer code, it is necessary to demonstrate its applicability in a variety of problems. The shock-capturing, finite-difference computational procedure (SCT)[1,2] has already been shown to have promise in predicting complex hypersonic flows. To further extend the applicability and usefulness of the SCT, this paper presents results of some recent studies that used this method. In addition, this opportunity is taken to present an extensive collection of experimental aerodynamic coefficients for symmetric biconic bodies at angles of attack.

The work presented here is divided into two parts. In the first part, the details of the shock layer surrounding a variation of the space shuttle/orbiter are calculated. The numerical solution is compared with experimental data in Mach 7.3 flow at 30° angle of attack. The second part, which consists of two sections, evaluates the aerodynamics of blunted biconic bodies at angles of attack up to 20°. In the first section, changes in the body aerodynamics due to geometric variations, including the effects of nose bluntness, forcone and aft-cone angle, and cone juncture location, are

examined at Mach number 8. In the second section, normal force, pitching moment, and center-of-pressure calculations are presented for a baseline biconic configuration over a Mach number range of 5 to 20. In both sections, the numerical results are compared with appropriate wind-tunnel force-and-moment data which were obtained at Mach numbers 5, 8, 10, 14, and 16.

Computational Aspect of the Problem

The conservation equations have been given previously[1,2] so they are not repeated here; however, the computational plane has been changed in the present work and is discussed next. In the calculational procedure, the governing partial differential equations for cylindrical coordinates are normalized between the body and peripheral shock, which is treated as a sharp discontinuity. The conservation-law form of the equations is used. Thus, the flow between the body and the outermost shock is treated in a shock-capturing fashion and, therefore, allows for the correct formation of secondary internal shocks such as a crossflow shock, wing shock, or canopy shock. Since the inviscid flow is entirely supersonic, the governing gasdynamic equations are hyperbolic. Thus, given a starting solution, there follows a well-posed initial-value problem. The starting solutions of this paper were produced using an inverse method[3] for the blunt nose, followed by a method-of-characteristics technique to march the supersonic region to the end of the nose cap and into an axis normal, initial data plane for the SCT code. The governing equations are then integrated numerically downstream from this plane using the second-order, noncentered, finite-difference algorithm of MacCormack.[4] Previous results[1,2] have demonstrated the feasibility of applying the shock-capturing technique to the complicated configurations and flows considered in this paper.

The flowfields about the configurations studied feature the formation of regions of highly rotational flow, i.e., entropy layers resulting from the blunt nose. As the solution is marched downstream, the entropy layer begins to converge on the body. Numerical methods which employ a fixed grid begin to lose resolution in such a layer because of the rapid changes in the gradients of the dependent variables. Nonphysical

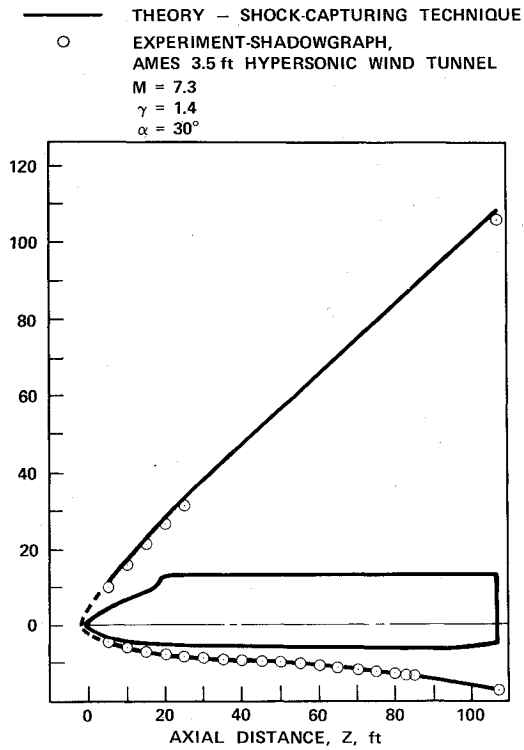

Fig. 1 Profile view, shock location, orbiter body.

oscillations and possible instabilities can occur unless some special treatment is instituted, e.g., Thomas'[5] approach of clustering points in such regions via an independent-variable transformation, or by entropy layer relaxation. Such regions can exist on biconic bodies and on the windward side of the space shuttle. In the present work, an independent-variable transformation of the radial coordinate is applied to cluster points near the body; a free parameter, ω, is introduced to adjust the degree of clustering.

Similarly, clustering in the circumferential direction is often needed to resolve regions with large gradient variations. For example, in the vicinity of the wing tip of the space shuttle flying at supersonic velocities, the flow variables change rapidly in the crossflow direction. On both the biconic bodies and the space-shuttle configuration at large angles of attack, a crossflow shock wave forms on the lee side as a result of the required deceleration of the supersonic crossflow to zero at the plane of symmetry. To maintain the accuracy of the solution in such a region, an independent-variable transformation is applied in the circumferential or ϕ-direction to cluster points at a given meridional location, ϕ_{cluster}. The degree of clustering is controlled by the parameter, β.

The computational plane under the transformations discussed above and for a cylindrical coordinate system is obtained as follows: Let Z be a straight axis oriented along the longitudinal centerline of the vehicle and ϕ the meridional angle measured from some reference plane. The distance between the body and outer shock is normalized by a transformation of the radial variable r. The vehicle body geometry and the location of the outer or peripheral shock are represented, respectively, by functions of the form

$$r_b = r_b(Z,\phi) \tag{1}$$

$$r_s = r_s(Z,\phi) \tag{2}$$

The function r_b is specified by the particular geometry, e.g., a) as in Ref. 2, or b) using a geometry description procedure developed by Batchelder[6] for biconic configurations; whereas r_s is determined as the equations are integrated. These functions result in a rectangular computational plane whose boundaries consist of the two planes of symmetry ($\phi = 0°$ and 180°), the body surface, and the peripheral shock surface.

The equations governing the independent variable transformation discussed above are

$$\zeta = Z \tag{3}$$

$$\xi(Z,r,\phi) = \frac{r - r_b(Z,\phi)}{r_s(Z,\phi) - r_b(Z,\phi)} \tag{4}$$

$$\tau(Z,r,\phi) = \begin{cases} \dfrac{1}{\omega}\sinh^{-1}(\xi \sinh \omega) & \omega > 0 \\ \xi & \omega = 0 \end{cases} \tag{5}$$

$$\eta(\phi) = \begin{cases} \pi\left\{C + \dfrac{1}{\beta}\sinh^{-1}\left[\left(\dfrac{\phi}{\phi_{\text{cluster}}} - 1\right)\sinh(\beta C)\right]\right\} & \beta > 0 \\ \phi & \beta = 0 \end{cases} \tag{6}$$

where

$$C = \frac{1}{2\beta}\ln\left[\frac{1 + (e^{\beta} - 1)\dfrac{\phi_{\text{cluster}}}{\pi}}{1 - (1 - e^{-\beta})\dfrac{\phi_{\text{cluster}}}{\pi}}\right] \tag{7}$$

and β and ω are free parameters satisfying β and $\omega \geq 0$. The larger the value of β or ω, the closer the points are clustered. In this study, β usually varied between 0 and 6.

The shuttle/orbiter calculations were performed on an IBM 360/67 linked with a cathode-ray display tube (CRT) and on a CDC 7600. The calculations are readily controlled and efficiently performed when using the CRT with its man-machine interactive capability, thus establishing a refined procedure to follow on the much faster, noninteractive CDC 7600. In the biconic calculations, which were performed on a CDC Cyber 74, 10 radial field points and 12 meridional points were used. Clustering was not used for any of the biconic cases presented here. Typical central processor times for the CDC Cyber 74 system ranged from 95 sec for the 20% blunt configuration at an α of 2.5°, to 644 sec for the 5% blunt body at an α of 20°.

Results for Space Shuttle/Orbiter

Results for a blunt-nosed orbiter are compared with experimental data for a 7.3 Mach number, a 30° angle of attack, and a 1.4 ratio of specific heats. During the calculations, the number of radial points was varied, up to a maximum of 22. The number of meridional planes also varied, up to a maximum of 37. During the integration, points were clustered circumferentially in the region of the largest meridional gradient changes.

The computed profile and planform peripheral shock waves are shown in Figs. 1 and 2. A comparison with experimental data for the profile view is shown in Fig. 1. The predicted windward shock wave location agrees well with the experimental results. On the leeward side, the difference between the experimental and computed shock location is most likely due to the differences between the wind-tunnel model geometry and the numerical simulation of this geometry in the calculations.

The shock shape at a meridional angle of 81° is presented in Fig. 2 in order to exhibit the characteristics of the wing protruding from the body. The important feature is the collision of the bow shock with the wing shock. After this interaction, the wing shock is very close to the leading edge due to its small radius of curvature. This causes the step size to be very small throughout this region, which, in turn, increases the computation time.

In this and other calculations using the 45° swept wing configuration, there is a small region after the intersection of the bow shock and wing shock where the axial component of the flow is subsonic. This axially subsonic Mach number invalidates the marching procedure.

In order to circumvent the problem, a "fix" was made which modified the local Mach number to make it supersonic again by adjusting the local value of the total enthalpy. Even though this is not physically correct, it is preferred in order to expedite the calculation. Investigation has shown that the axial Mach number is so close to unity that adjusting it to just above 1 has little effect on the solution.

Figure 3 shows the longitudinal surface pressure distributions for the windward ($\phi = 0°$) and leeward ($\phi = 180°$) meridians. These are compared with experimental data which were obtained from tests in the Ames Research Center 3.5-Foot Hypersonic Wind Tunnel. The differences near the nose may be caused by a variation between the simulated and actual body shapes, allowing the pressure to expand faster in the

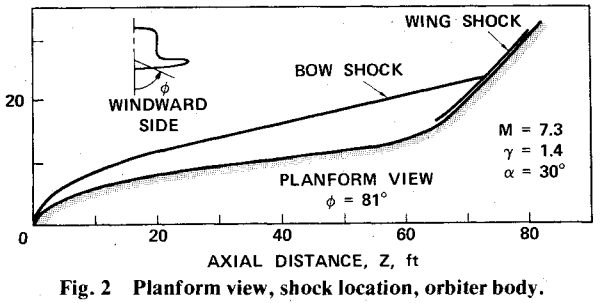

Fig. 2 Planform view, shock location, orbiter body.

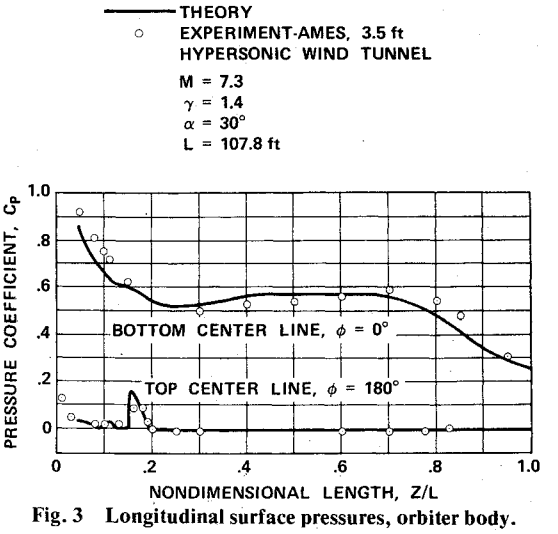

Fig. 3 Longitudinal surface pressures, orbiter body.

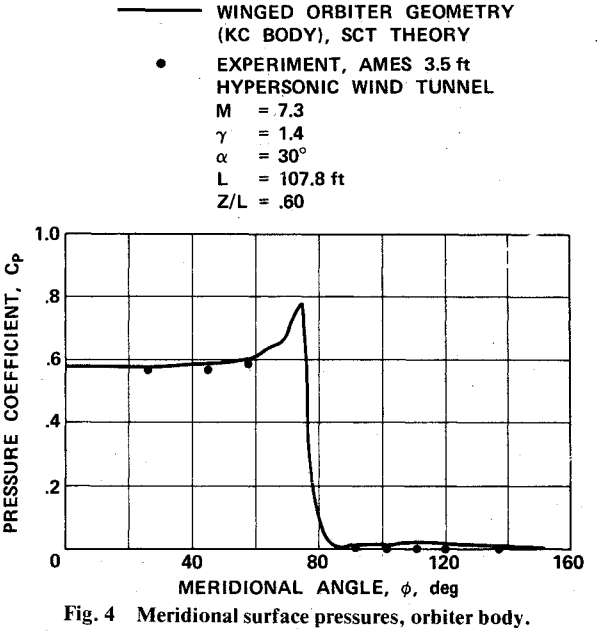

Fig. 4 Meridional surface pressures, orbiter body.

calculation of the flow over the simulated body. In the leeward plane ($\phi = 180°$), the pressure distribution follows that of the experiment. The rapid pressure rise, followed by the rapid decrease in the leeward plane, is the result of the canopy.

In Fig. 4, the predicted meridional pressure distribution is compared with experimental values for a normalized longitudinal station, $Z/L = 0.6$. At this Z/L station, the final 45° delta is just beginning to protrude into the flow, as seen by the rise in pressure near the $\phi = 74°$ plane. A comparison between the prediction and the available experimental points at this Z/L station indicates good agreement.

Results for Blunt-Nosed Biconic Bodies

The parametric study of the aerodynamics of blunt-nosed biconic bodies encompasses the effects of Mach number, nose bluntness, fore and aft cone angles, and biconic juncture location. Figure 5 illustrates the configuration variations which have been evaluated. The configuration selected as the baseline body for the study is designated as 15/8/5/50. These four sets of digits denote, respectively, a nose-to-base bluntness ratio, R_N/R_B, of 15%, a forecone half-angle, θ_F, of 8°, an aft cone half-angle, Θ_A, of 5°, and biconic juncture station, BK/L_V, at 50% of the virtual length, L_V, of the aft cone.

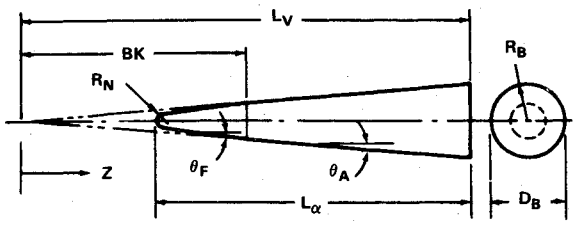

1. R_N/R_B (%) = 5, 10, 15, 20;
2. θ_F = 8°, 9°, 9.75°, 11°, 14°
3. θ_A = 5°, 6°
4. BK/L_V (%) = 50, 60

Fig. 5 Biconic configuration parameters.

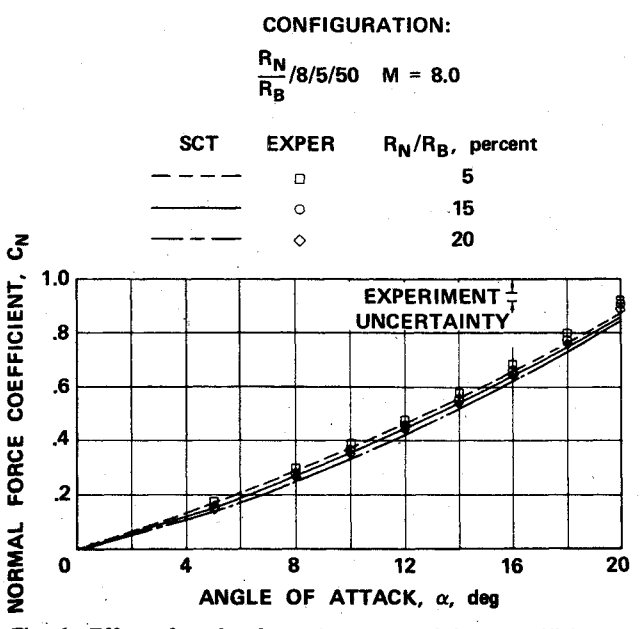

Fig. 6 Effect of angle of attack on normal force coefficients for varying nose bluntnesses.

The local body pressures calculated by the McDonnell Douglas Astronautics Co. version of the NASA SCT code have been integrated[6] to provide force and moment coefficients. Because the shock-capturing calculation actually provides only the load contribution of the biconic frustum starting with the nose tangency station, a supplementary computation was performed using a curve-fitting code[7] based on a standard calculation[3] to give the small increment due to the hemispherical nose cap. The results are presented in terms of a standard normal force coefficient, C_N, pitching moment coefficient, C_m, and center-of-pressure location Z_{CP}/L_V.

Table 1 Experimental program on biconic bodies

Mach number, M	Test facility	Body base diameter, D_B (in.)	Length Reynolds number, $Re_{L_\alpha} \times 10^{-6}$	Forced transition
5.04	AEDC-VKF Tunnel A	8.00	17.9	Yes
8.00	AEDC-VKF Tunnel B	8.00	9.7	Yes
10.13	AEDC-VKF Tunnel C	8.00	6.7	Yes
14.2	ARL 20-Inch Hypersonic Tunnel	3.00	0.6	No
16.2	AEDC-VKF Tunnel F	4.00	1.3	No

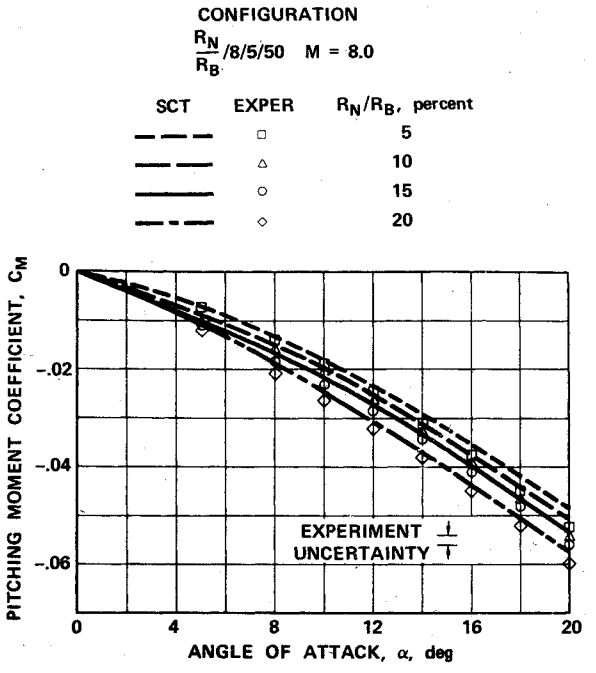

Fig. 7 Effect of angle of attack on pitching moment coefficient for varying nose bluntnesses.

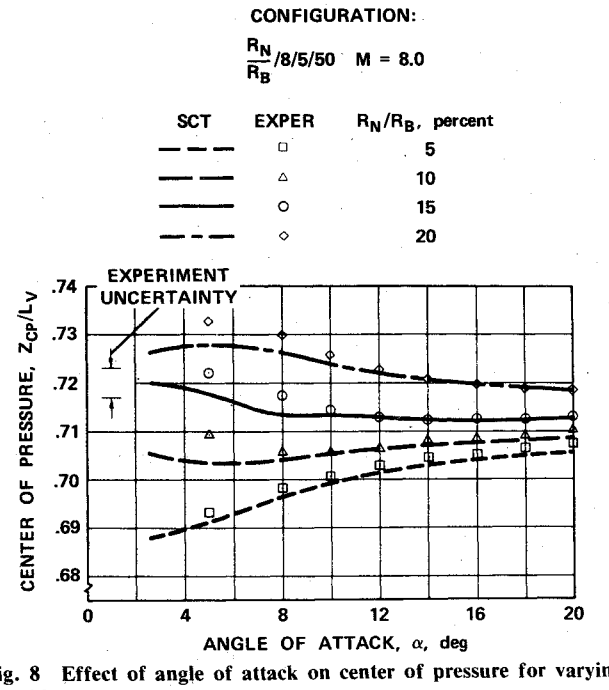

Fig. 8 Effect of angle of attack on center of pressure for varying nose bluntnesses.

The numerical results are compared with wind-tunnel data obtained in a series of force and moment tests on biconic models. These tests were performed in the Arnold Engineering Development Center (AEDC), Von Karman Facility (VKF), Tunnels A, B, C, and F at Mach numbers 5, 8, 10.1, and 16.2, respectively, and in the United States Air Force Aerospace Research Laboratories (ARL) 20-Inch Hypersonic Wind Tunnel at Mach number 14.2. Some details of the experimental program are shown in Table 1.

Effects of Geometry Variations at Mach Number 8

Extensive numerical and experimental studies have been made of variations in aerodynamics due to biconic geometry variations. All wind-tunnel data reported here for this set of

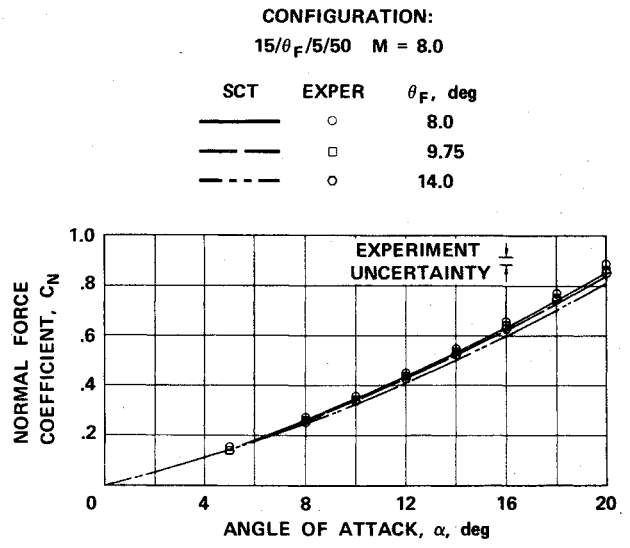

Fig. 9 Effect of angle of attack on normal force coefficient for varying forecone angles.

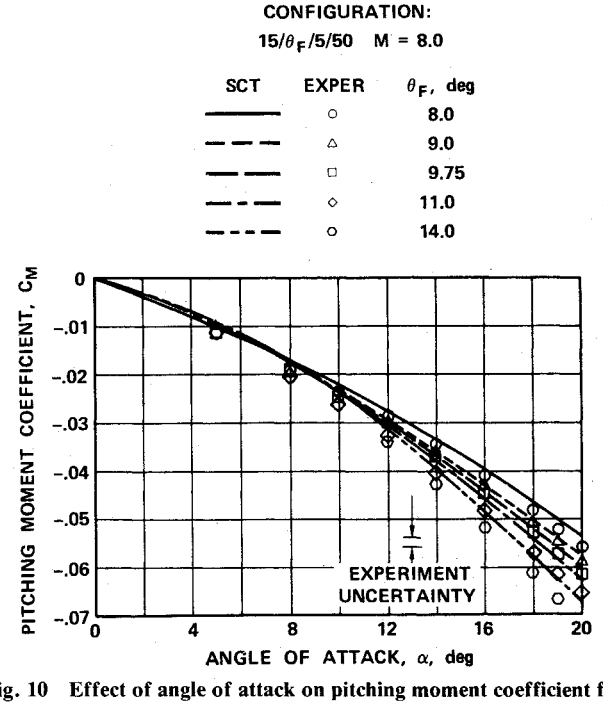

Fig. 10 Effect of angle of attack on pitching moment coefficient for varying forecone angles.

geometry comparisons were obtained in the AEDC Tunnel B at Mach 8.

Figures 6 and 7, respectively, give C_N and C_m vs angle of attack, α, up to 20° for nose-radius to base-radius bluntness ratios of 5, 10, 15, and 20%. The 10% bluntness calculations and data have been omitted from Fig. 6 for clarity; if present, they would fall in proper sequence. The calculated values of both coefficients consistently fall slightly lower than the experimental data points at α's above 5°.

For C_m at $\alpha = 20°$, the calculation (Fig. 7) for the 5% blunt body is 7% below the data, while that for the 20% blunt body is 4% lower. These discrepancies are somewhat greater than the probable uncertainty of the experimental data, and they are considered to be real. The test data trends proved repeatable over an extended time period encompassing several separate series of tests.

While the SCT and experimental values of C_N and C_m differ slightly, the center-of-pressure locations for the various

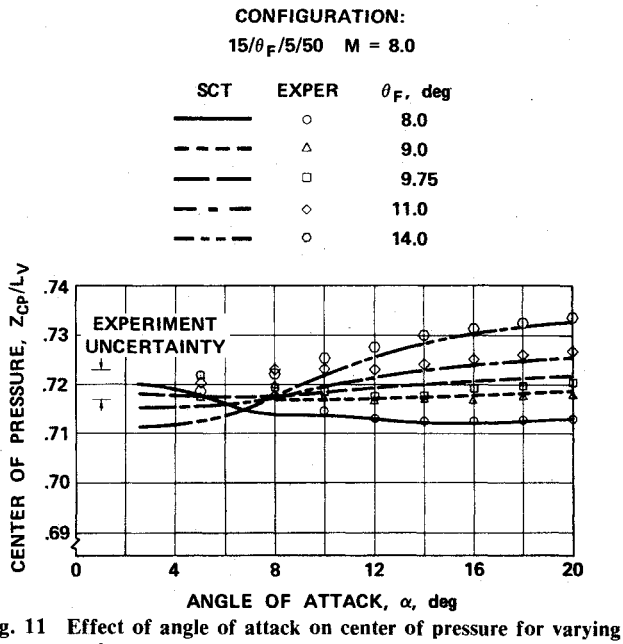

Fig. 11 Effect of angle of attack on center of pressure for varying forecone angles.

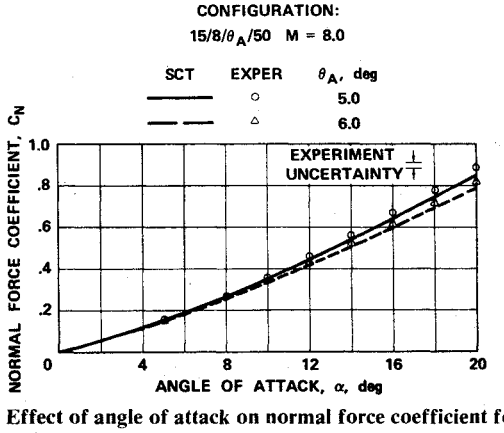

Fig. 12 Effect of angle of attack on normal force coefficient for two aft cone angles.

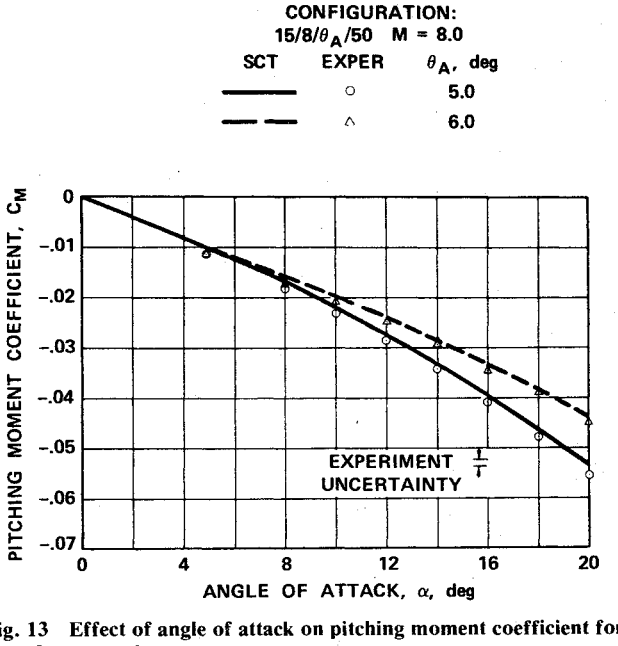

Fig. 13 Effect of angle of attack on pitching moment coefficient for two aft cone angles.

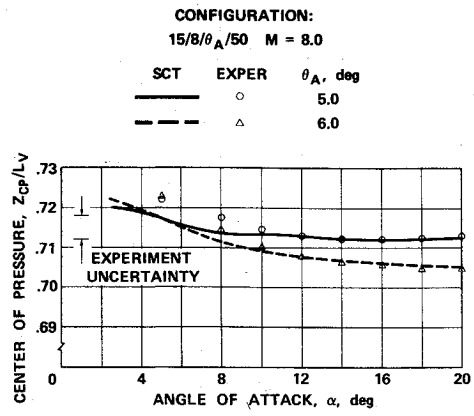

Fig. 14 Effect of angle of attack on center of pressure for two aft cone angles.

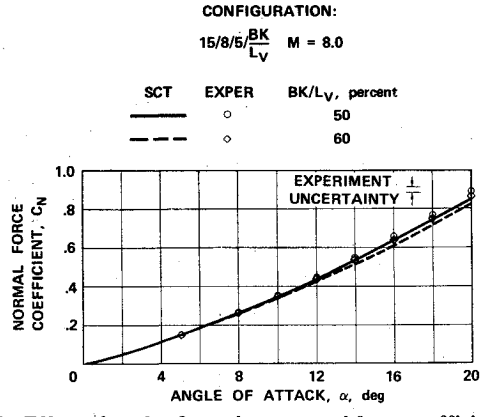

Fig. 15 Effect of angle of attack on normal force coefficient for two biconic juncture locations.

nose bluntnesses, which are given in Fig. 8, indicate that the load distributions calculated by the SCT code agree well with experiment at high α. The deviations at the lower α's may be associated with leeside viscous effects in the test data, which occur as the aft cone, and then the forecone, enter the shadow region during the angle-of-attack cycle.

Figures 9-11 show the SCT calculations and experimental data for forecone half-angles of 8.0°, 9.0°, 9.75°, 11.0°, and 14.0°. Two intermediate θ_F's have been omitted from Fig. 9 for clarity. Again, the SCT curves show values of C_N in Fig. 9, and of C_m in Fig. 10 which are slightly smaller in magnitude than the experimental results. At $\alpha = 20°$, the pitching moment is 4% low for $\theta_F = 8°$ and 7% low for $\theta_F = 14°$.

Figure 11 indicates that the centers of pressure agree at high α's, although there are significant discrepancies at low α's. The deviation between SCT and test data appears to persist to at least a 14° angle of attack for the 14° forebody, and to an α of around 12° for the 11° body. Agreement is good down to $\alpha = 10°$ for the 8°, 9°, and 9.75° forebodies. This tendency is consistent with postulated significant leeside viscous phenomena.

Figures 12-14 show the predicted vs measured values of C_N, C_m, and Z_{CP}/L_V, respectively, for aft cone half-angles of 5° and 6°. The effect of varying biconic juncture station from 50% to 60% of L_V is presented in Figs. 15-17, which, again, show predicted vs measured C_N, C_m, and Z_{CP}/L_V. In both cases, the comparison of SCT results to experimental values shows trends similar to those already discussed.

Effects of Mach Number

Figures 18 and 19 present the normal force and pitching moment coefficients for the baseline biconic configuration at

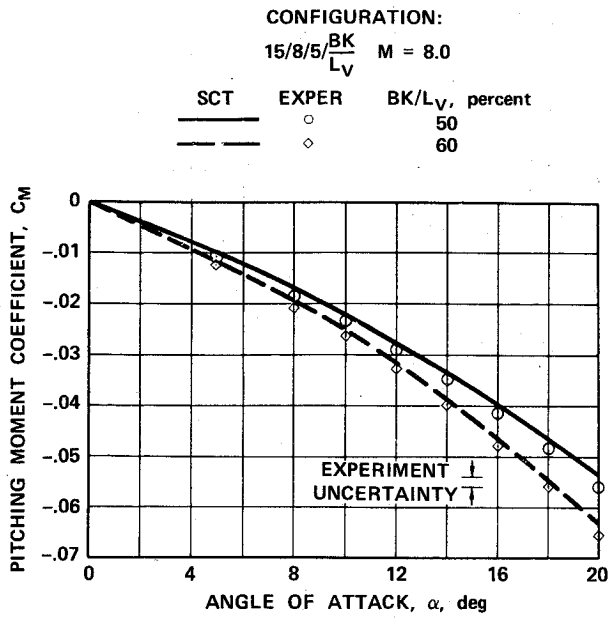

Fig. 16 Effect of angle of attack on pitching moment coefficient for two biconic juncture locations.

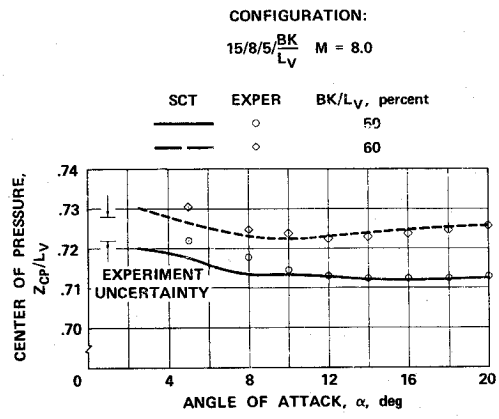

Fig. 17 Effect of angle of attack on center of pressure for two biconic juncture locations.

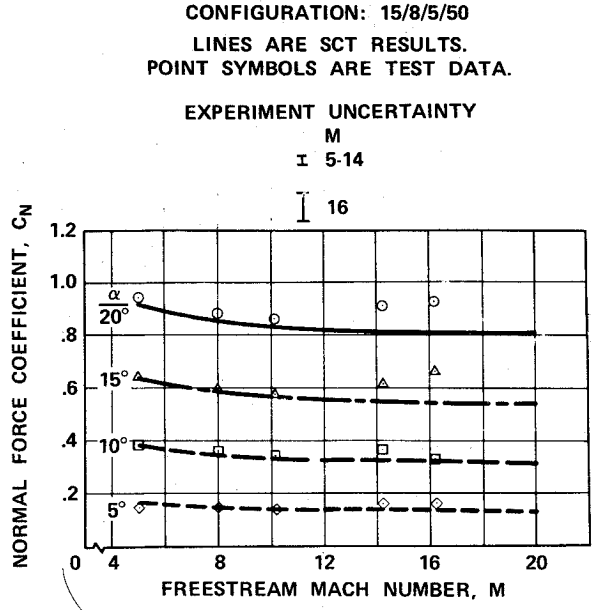

Fig. 18 Mach number effect on normal force coefficient for varying angle of attack.

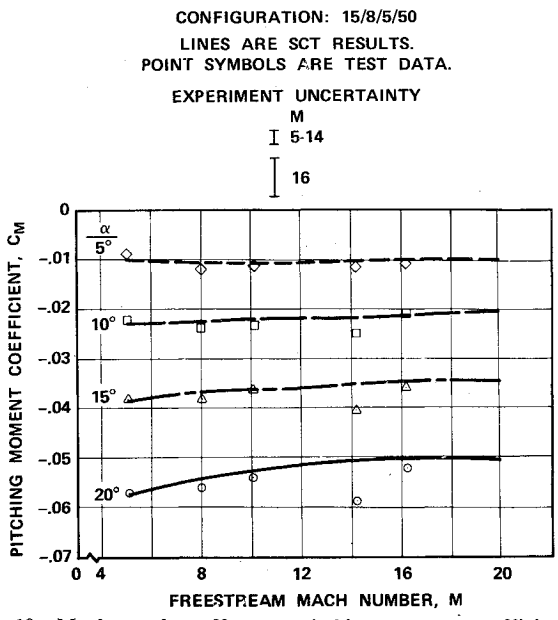

Fig. 19 Mach number effect on pitching moment coefficient for varying angle of attack.

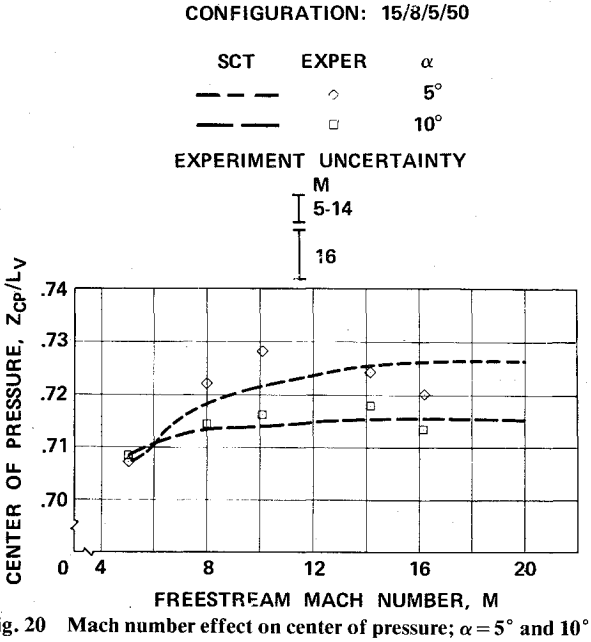

Fig. 20 Mach number effect on center of pressure; $\alpha = 5°$ and 10°.

5°, 10°, 15°, and 20° angles of attack as a function of Mach number. The SCT calculations were made for a series of Mach numbers between 5 and 20, and these are compared with the wind-tunnel data, which range from Mach 5 to 16.2. The comparisons indicate good agreement, except for some of the high-α, high-M points, where particular experimental data points exhibit apparent anomalies. As indicated in Table 1, the tests at Mach numbers 14.2 and 16.2 were conducted at model length Reynolds numbers which were an order of magnitude smaller than those for the three lower Mach numbers. These higher Mach number boundary layers were laminar and too stable to attempt to trip, whereas turbulence was forced just aft of the nose cap at the three lower Mach numbers. Thus, it is possible that viscous effects may be contributing to the disagreement between the low Reynolds number Mach 14.2 and 16.2 test data and the inviscid-flow SCT calculations.

The predicted and measured centers of pressure for the baseline biconic configuration as a function of Mach number are examined at $\alpha = 5°$ and 10° in Fig. 20, and at $\alpha = 15°$ and 20° in Fig. 21. To display the details of the trends, a very sensitive Z_{CP}/L_V plot scale was selected relative to the experimental uncertainty bands.

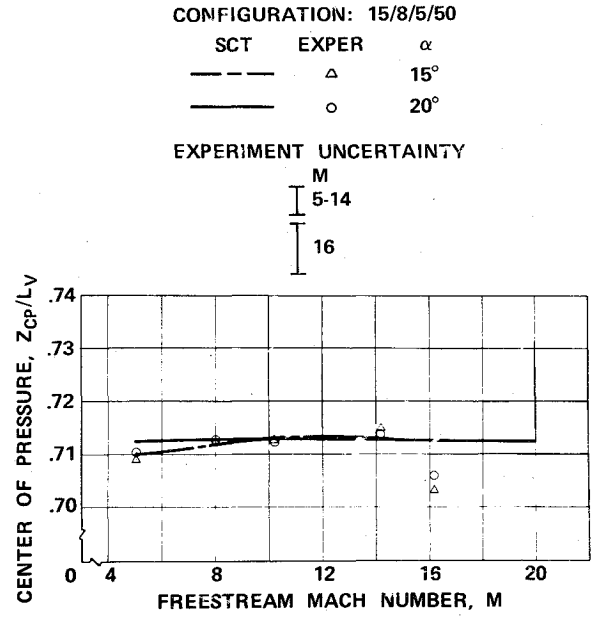

Fig. 21 Mach number effect on center of pressure; $\alpha = 15°$ and 20°.

An interesting application of the SCT code[6] has involved the use of a source flowfield option to adjust the Mach 16.2 test data, which were obtained in a conical nozzle in the AEDC Tunnel F. Incremental corrections calculated by the code were used to shift the C_N, C_m, and Z_{CP}/L_V test data measured in the source flowfield to the equivalent parallel-flow values shown here in Figs. 18-21. The resulting parallel-flow center of pressure is 0.0047 Z/L_V aft of the measured value at $\alpha = 5°$ and 0.0040 Z/L_V aft at $\alpha = 20°$.

Conclusions

The results of these studies indicate that the shock-capturing, finite-difference approach (SCT) can successfully solve flows over complex bodies such as the space shuttle through a wide range of flow conditions. Codes based on the SCT have been used to find shock shapes and locations, detailed surface pressure distributions, and body total loads, moments, and centers of pressure. The results of the parametric configuration analysis reported here for the blunted biconics show that the SCT can be a valuable tool in vehicle design studies.

References

[1] Kutler, P., Lomax, H., and Warming, R. F., "Computation of Space Shuttle Flow Fields Using Noncentered Finite-Difference Schemes," *AIAA Journal*, Vol. 11, Feb. 1973, pp. 196-204.

[2] Kutler, P., Reinhardt, W. A., and Warming, R. F., "Multi-Shocked, Three-Dimensional Supersonic Flowfields with Real Gas Effects," *AIAA Journal*, Vol. 11, May 1973, pp. 657-664.

[3] Inouye, M., Rakich, J. V., and Lomax, H., "A Description of Numerical Methods and Computer Programs for Two-Dimensional and Axisymmetric Supersonic Flow Over Blunt-Nosed and Flared Bodies," NASA TN D-2970, Aug. 1965.

[4] MacCormack, R. W., "The Effect of Viscosity in Hypervelocity Impact Cratering," AIAA Paper 69-354, Cincinnati, Ohio, 1969.

[5] Thomas, P. D., Vinokur, M., Bastianon, R. A., and Conti, R. J., "Numerical Solution for Three-Dimensional Inviscid Supersonic Flow," *AIAA Journal*, Vol. 10, July 1972, pp. 887-894.

[6] Batchelder, R. A., "Kutler Inviscid Supersonic Three-Dimensional Flow Program P2871 Input/Output Guide," McDonnell Douglas Astronautics Company, Huntington Beach, Calif., MDC G5799, May 1975.

[7] Timmer, H. G. and Stokes, T. R., "Rapid Prediction of Hypersonic Aerodynamic Characteristics: Computer Program F218," McDonnell Douglas Astronautics Company, Huntington Beach, Calif., DAC-62432, Dec. 1968.